



Full length article

## Part II: Experimental verification of computationally predicted preferential oxidation of refractory high entropy ultra-high temperature ceramics

Lavina Backman<sup>a,\*</sup>, Joshua Gild<sup>b</sup>, Jian Luo<sup>b</sup>, Elizabeth J. Opila<sup>a</sup>

<sup>a</sup>Department of Materials Science and Engineering, University of Virginia, Charlottesville VA 22904, United States

<sup>b</sup>Department of NanoEngineering, Materials Science and Engineering Program, University of California-San Diego, La Jolla, CA, United States

### ARTICLE INFO

#### Article history:

Received 24 December 2019

Revised 30 June 2020

Accepted 2 July 2020

Available online 7 July 2020

#### Key words:

High temperature oxidation

High entropy alloys

Ultra-high temperature ceramics

High entropy carbides

High entropy borides

Refractory

### ABSTRACT

Refractory high entropy materials have garnered significant research interest due to their potential ability to fill a need in high temperature structural applications. However, challenges remain with respect to designing for oxidation resistance. A knowledge gap exists with respect to a rigorous understanding of the mechanisms driving oxidation processes unique to high entropy materials. This work provides an experimental complement to a companion publication, which outlines analytical and computational thermodynamic approaches that are envisioned to aid the design of refractory high entropy materials containing group IV (Hf, Zr, Ti) and group V (Ta, Nb) constituents. In this work, (Hf<sub>0.2</sub>Zr<sub>0.2</sub>Ti<sub>0.2</sub>Ta<sub>0.2</sub>Nb<sub>0.2</sub>) carbide and diboride specimens were exposed at 1700°C in 1% O<sub>2</sub> for 5 min. Experimental results show good agreement with the computational predictions for the same temperature, despite differences in the overall morphology of the oxidized regions. The carbide formed porous oxides, while the diboride formed a denser external scale. Oxidation products are dominated by group IV oxides, depleting the underlying materials, which were found to consist of primarily group V carbides and borides respectively. The results provide a first look at the oxidation of high entropy UHTCs at ultra-high temperatures and validate the preferential nature of high entropy material oxidation predicted by the computational approach developed for the study of this new class of materials.

© 2020 Acta Materialia Inc. Published by Elsevier Ltd. All rights reserved.

### 1. Introduction

Ultra-high temperature ceramics (UHTCs), most notably refractory metal carbides, nitrides and borides, may hold the key to advancement in hypersonic flight technology. UHTCs exhibit melting temperatures exceeding 3000°C, making them appropriate candidates to withstand the extreme temperatures experienced by the leading edges of the vehicle during hypersonic flight. However, their propensity to react rapidly with oxygen limits their sustained application [1,2]. Researchers have attempted to address this limitation through the modification of well-understood systems. For instance, the addition of SiC to boride UHTCs, such as ZrB<sub>2</sub>, improves oxidation resistance [2–4] due to the formation of a liquid borosilicate glass layer. However, this layer will shear off at the speeds and temperatures encountered in hypersonic flight (maximum melting temperature for this layer occurs when the scale is

pure SiO<sub>2</sub> at 1723°C). Further, the active oxidation of silicon carbide at temperatures higher than 1600°C also precludes the use of silica formers for passivity [5]. High entropy ultra-high temperature ceramics (HE-UHTCs), an emerging class of materials [6–8], are of interest due to the potential to significantly expand the compositional breadth of UHTCs and the range of achievable properties. The design of an HE-UHTC will require not only the ability to form a single-phase solid solution but also to optimize the desired properties including oxidation resistance at ultra-high temperatures (>1700°C), the focus of this paper.

While several studies have been published on the observed oxidation behavior [9,10] of high entropy multi-principal component materials (of which high entropy alloys and ceramics are subsets), a rigorous treatment of the underlying mechanisms that control the oxidation behavior unique to high entropy materials have yet to be established. Prior work has shown that thermodynamic favorability plays a role in the assemblage of phases formed after exposure to the oxidizing environment [9,11], suggesting highly composition dependent oxidation behavior. A companion publication [12] proposes a method to predict the oxidation products in

\* Corresponding author.

E-mail addresses: [lb2ty@virginia.edu](mailto:lb2ty@virginia.edu) (L. Backman), [jgild@ucsd.edu](mailto:jgild@ucsd.edu) (J. Gild), [jluc@ucsd.edu](mailto:jluc@ucsd.edu) (J. Luo), [opila@virginia.edu](mailto:opila@virginia.edu) (E.J. Opila).

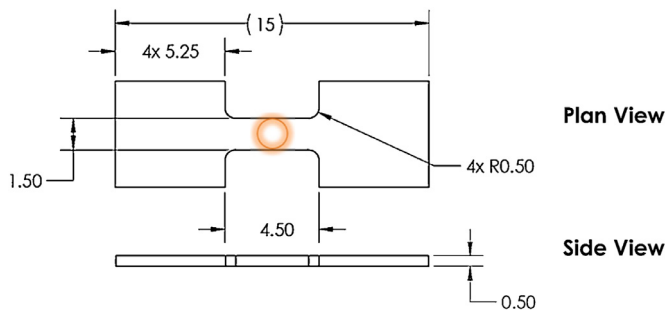


**Fig. 1.** Dogbone specimen configuration. The approximate hot zone, or pyrometer sighting zone (diameter 1.5 mm), is shown in orange. Dimensions shown are in millimeters (mm).

these complex, solid solution materials, with the goal of using these findings to inform new, oxidation-resistant designs for all non-oxide high entropy materials. The computational work simplifies real materials to the ideal solution model due to a lack of thermodynamic data to consider real systems. An experimental study is therefore needed to validate the predicted assemblage of oxide product and substrate phases. The objective of this work is to apply the previously developed computational approach to experimental oxidation of UHTC systems of interest in order to verify its predictions.

## 2. Methodology

Materials chosen for the study are carbides and borides containing group IV and group V elements: Hf, Zr, Ti, Ta and Nb. Hf and Zr carbides and diborides are UHTC candidates that form oxides with the highest melting temperatures [2]. Tantalum has been an extensively studied elemental addition for high temperature UHTCs [13–15], and in the context of this work, has the ability to form solid solutions with Hf and Zr based compounds. Next to group IV oxides, tantalum oxides also have the highest melting temperature among the species under consideration. The  $(\text{Hf}_{0.2}\text{Zr}_{0.2}\text{Ti}_{0.2}\text{Ta}_{0.2}\text{Nb}_{0.2})$  carbide and diboride were also among the first compositions for which single phase, UHTC solid solutions were made [6,16]. The approach outlined in the companion publication [12] was used to calculate the oxide and resulting substrate composition at 1700°C for the carbide and boride. Note that the partial pressure of oxygen is not defined as an input but is a result from the free energy minimization calculations given the initial condition of a carbide (or boride) solid solution at equilibrium with an oxide solid solution.

The  $(\text{Hf}_{0.2}\text{Zr}_{0.2}\text{Ti}_{0.2}\text{Ta}_{0.2}\text{Nb}_{0.2})\text{C}$  specimen tested in this work was prepared by high energy ball milling and spark plasma sintering (SPS) commercially available powders (Alfa Aesar Haverhill, MA) [16,17]. The  $(\text{Hf}_{0.2}\text{Zr}_{0.2}\text{Ti}_{0.2}\text{Ta}_{0.2}\text{Nb}_{0.2})\text{B}_2$  specimen was prepared by borocarbothermal reduction [18], followed by SPS consolidation. The sintered samples were machined at Bomas Machine Specialties (Somerville, MA) into 0.5 mm thick dogbone specimens shown in Fig. 1. Samples cut from the same sintered pucks were mounted, polished and characterized before oxidation via scanning electron microscopy (SEM, FEI Quanta 650, FEI-Thermo Fisher Scientific, Hillsboro, Oregon), energy dispersive spectroscopy (EDS, Oxford Instruments Aztec X-Max<sup>N</sup> 150, Concord, MA) and X-ray diffraction (XRD, PANalytical X'Pert Pro-MPD or PANalytical Empyrean, Almelo, The Netherlands).

These dogbone specimens were then loaded into a resistive heating system, modified from Karlsdottir and Halloran [19], and Shugart and Opila [20], schematic shown in Fig. 2. The samples were heated to the desired temperature (nominally 1700°C in this study) through Joule heating. The temperature was chosen as it is

the minimum temperature in the ultra-high temperature regime, wherein strategies to promote formation of  $\text{SiO}_2$  are not expected to be effective. The temperature was controlled by a proportional-integral-derivative (PID) controller and an emissivity correcting one-color pyrometer (Pyrofiber Lab PFL-0865–0790–2500C311, Pyrometer Instrument Company, Ewing Township, NJ). The pyrometer sights on an approximately 1.5 mm diameter zone in the middle of the dogbone specimen (Fig. 1). The mean temperatures measured by the pyrometer in this zone during the oxidation test for the carbide was  $1715 \pm 34.4^\circ\text{C}$ , and the diboride  $1700 \pm 27^\circ\text{C}$ . The samples were ramped to temperature in flowing ( $\sim 1$  L/min) ultra-high purity argon (2 vol-ppm  $\text{O}_2$  impurity max, Praxair, Danbury, CT), and certified 1 vol%  $\text{O}_2$  (balance argon) gas (Praxair, Danbury, CT) was turned on ( $\sim 1$  L/min) once the test temperature was achieved. Isothermal oxidation exposures were conducted for 5 min from the time the oxidizing gas began to flow. The low partial pressures of oxygen used result in lower oxidation rates allowing for longer exposures and time dependent studies which will be described in a future publication [Backman L, Gild J., Harrington T., Vecchio K., Luo J. and Opila, E.J., manuscript in preparation]. After oxidation, the oxide morphology in both plan view and cross section were characterized using the Everhart Thornley detector (ETD), circular backscatter detector (CBS) and ion conversion and electron (ICE) detector in the SEM, and the composition characterized using EDS. The oxide phases were identified using XRD. The samples were then manually fractured across the hot zone, and the cross-sections were examined in an SEM. Focused ion beam (FIB) milling (Helios UC G4, Thermo Fisher Scientific, Hillsboro, Oregon) was used to obtain samples for imaging and EDS analysis. The schematic shown in Fig. 3 shows the location of the FIB lift-out.

## 3. Results

### 3.1. Baseline material

The  $(\text{Hf}_{0.2}\text{Zr}_{0.2}\text{Ti}_{0.2}\text{Ta}_{0.2}\text{Nb}_{0.2})\text{C}$  exhibited  $\sim 99\%$  relative density, no open porosity and  $\sim 4$  vol% retained oxide contamination from the starting powders (Fig. 4) and was synthesized at the University of California, San Diego (synthesis and results from similar samples described in Harrington et al. [16,17]). The single phase  $(\text{Hf}_{0.2}\text{Zr}_{0.2}\text{Ti}_{0.2}\text{Ta}_{0.2}\text{Nb}_{0.2})\text{B}_2$  was synthesized by consolidating borocarbothermally reduced powders by Gild et al. as described in their publication [18] and exhibited  $\sim 99\%$  relative density with  $\sim 4$  vol%  $\text{B}_4\text{C}$  retained from processing and a minor amount ( $< 1$  vol%) of rock-salt carbide. The retained oxides in the carbide and the secondary phases in the diboride are randomly dispersed. A baseline set of EDS maps of polished cross-sections is provided here in Figs. 4 and 5, before oxidation, for reference and comparison to results after oxidation. The distribution of elements is uniform, except for the retained hafnium and zirconium oxides in the otherwise single-phase carbide material. These oxide impurities originate from the surface of the raw material powders used and are difficult to reduce due to their thermodynamic favorability.

### 3.2. Carbides: after oxidation

Fig. 6 shows light optical and back-scattered electron images of the exposed  $(\text{Hf}_{0.2}\text{Zr}_{0.2}\text{Ti}_{0.2}\text{Ta}_{0.2}\text{Nb}_{0.2})\text{C}$  specimen. The hot zone can be discerned by a dark gray region in the middle of the specimen surrounded by a lighter gray oxide (Fig. 6(c) and (d)). These images highlight the temperature gradients inherent in the experimental set-up, which will be addressed in more detail in future work. This paper focuses on results obtained from the center of the hot zone, well within the boundary of the pyrometer sighting zone.

At least two phases can be discerned on the surface from the microstructure in the hot zone as shown in Fig. 7: one that is

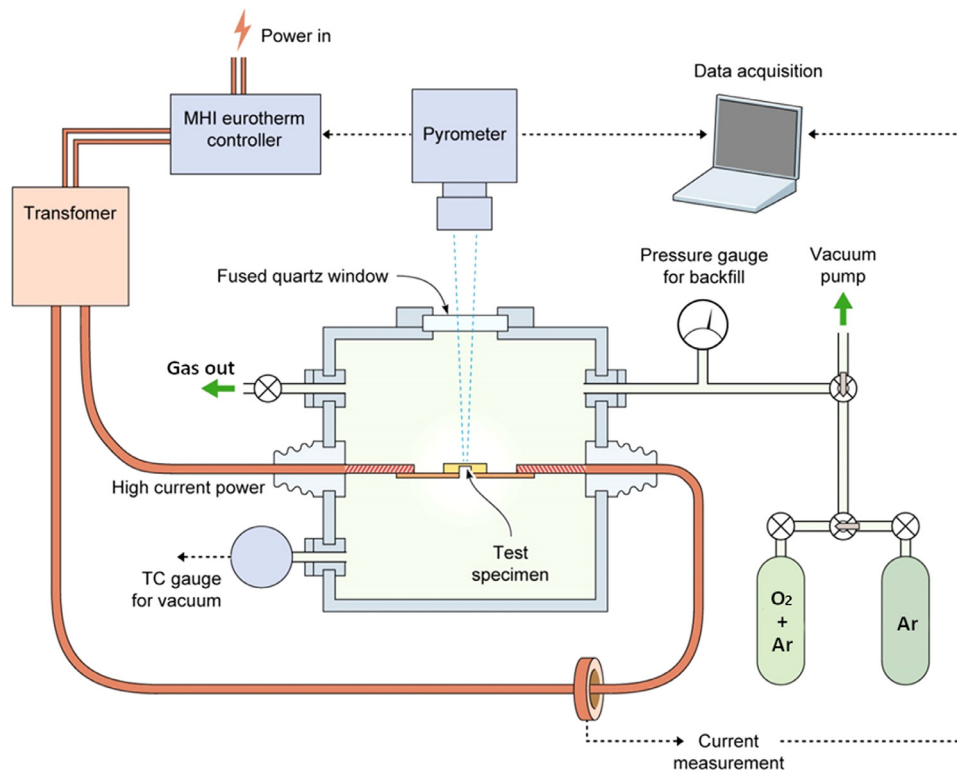


Fig. 2. Schematic of the resistive heating experimental set-up. Specimen shown is of different configuration for clarity.

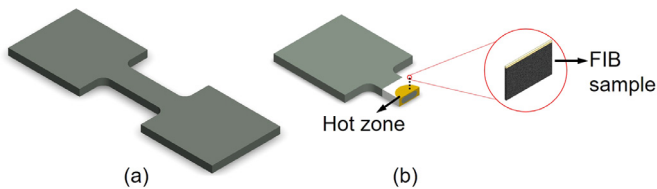


Fig. 3. Schematic showing the (a) unoxidized dogbone specimen, (b) oxidized dogbone fractured in the middle of the hot zone, with the hot zone shown in yellow and linked to the FIB lift-out with the approximate location in the hot zone. Total lift-out dimensions are approximately  $20\ \mu\text{m} \times 30\ \mu\text{m} \times 1\ \mu\text{m}$  before the thinning process.

rich in the group IV elements, and the other rich in Ti, but now with increased Ta and, to a lesser extent, Nb. Fig. 8 shows the corresponding indexed X-ray diffraction pattern of oxide formed on  $(\text{Hf}_{0.2}\text{Zr}_{0.2}\text{Ti}_{0.2}\text{Ta}_{0.2}\text{Nb}_{0.2})\text{C}$ . The composition of Phase 1, bright

phase in Fig. 7, is consistent with a titanate,  $(\text{Hf,Zr})\text{TiO}_4$ . The rounded morphology of the second phase could be indicative of the occurrence of melting. The composition and morphology of Phase 2, dark gray in Fig. 7, is a good match for  $\text{TiTa}_2\text{O}_7$ , which melts at  $1674^\circ\text{C}$  [21]. XRD data shown in Fig. 8 indicate other possible oxide phases, listed in Table 1. It should be noted that XRD analysis of the oxidized specimens in this study provide an indication of the likely phases present, but multiple overlaps make conclusive analysis difficult. Substitution of elements from the same periodic group are also likely, indicated in the third column shown in Table 1. Finally, the carbide was found to oxidize intergranularly (Figs. 9 and 10), with the subsurface oxides having different compositions compared to that on the surface; the other phases detected via XRD may be present in these regions.

Fig. 9 shows the ion conversion and electron (ICE) detector secondary electron (SE) image and EDS maps of oxide scale fracture

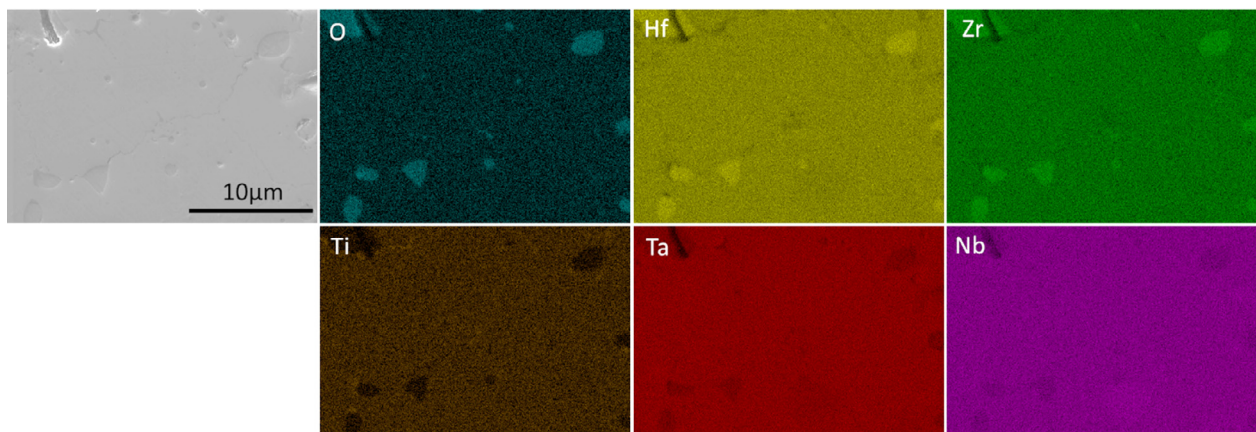
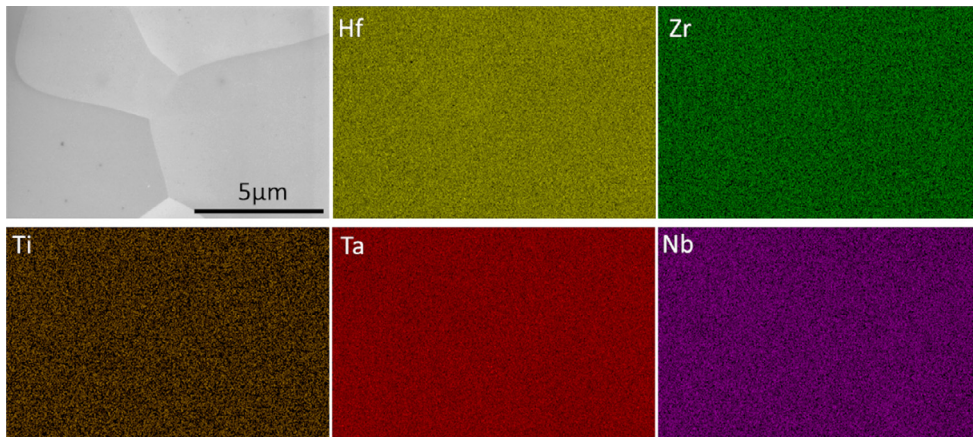
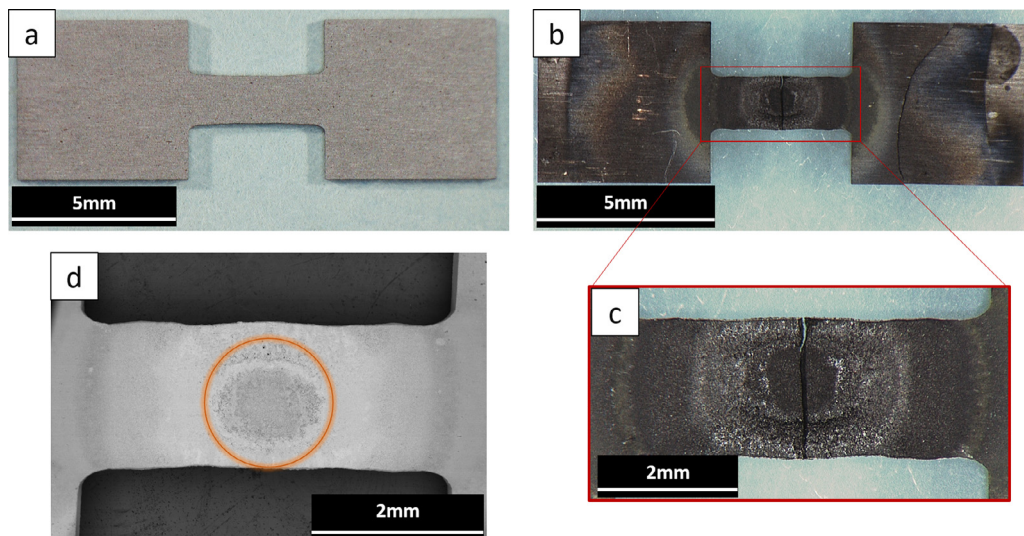


Fig. 4. Polished cross-sections of  $(\text{Hf}_{0.2}\text{ZrTi}_{0.2}\text{Ta}_{0.2}\text{Nb}_{0.2})\text{C}$  before exposure to oxygen at ultra-high temperatures. Secondary electron image and EDS maps showing elemental distribution of oxygen, hafnium, zirconium, titanium, tantalum, and niobium.



**Fig. 5.** Polished cross-sections of  $(\text{Hf}_{0.2}\text{ZrTi}_{0.2}\text{Ta}_{0.2}\text{Nb}_{0.2})\text{B}_2$  before exposure to oxygen at ultra-high temperatures. Secondary electron image and EDS maps showing elemental distribution of hafnium, zirconium, titanium, tantalum, and niobium..



**Fig. 6.** Plan view light optical images showing  $(\text{Hf}_{0.2}\text{ZrTi}_{0.2}\text{Ta}_{0.2}\text{Nb}_{0.2})\text{C}$  (a) before oxidation, (b–c) after oxidation at a nominal temperature of  $1700^\circ\text{C}$  in  $1\%\text{O}_2/\text{bal Ar}$  for 5 min, and manual fracture along the hot zone, and (d) back-scattered electron image in plan view of the hot zone before fracture. The orange circle is added to (d) to show the estimated size and location of the pyrometer sighting zone.

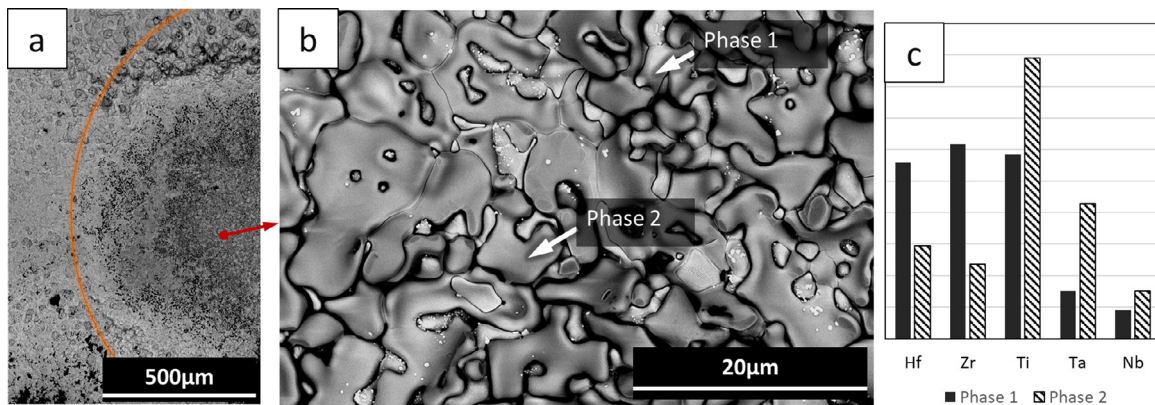


**Fig. 7.** Plan view images of  $(\text{Hf}_{0.2}\text{ZrTi}_{0.2}\text{Ta}_{0.2}\text{Nb}_{0.2})\text{C}$  after oxidation at a nominal temperature of  $1700^\circ\text{C}$  in  $1\%\text{O}_2/\text{bal Ar}$  for 5 min. (a) A low-magnification SEM image of the hot zone on one half of a dogbone (orange line indicates approximate boundary of the pyrometer sighting zone), (b) higher magnification, back-scattered electron image obtained at 5 kV of the microstructure in center of the pyrometer sighting zone (c) semi-quantitative composition of the two phases (bright and dark gray) apparent in this region from EDS obtained at 10 kV.

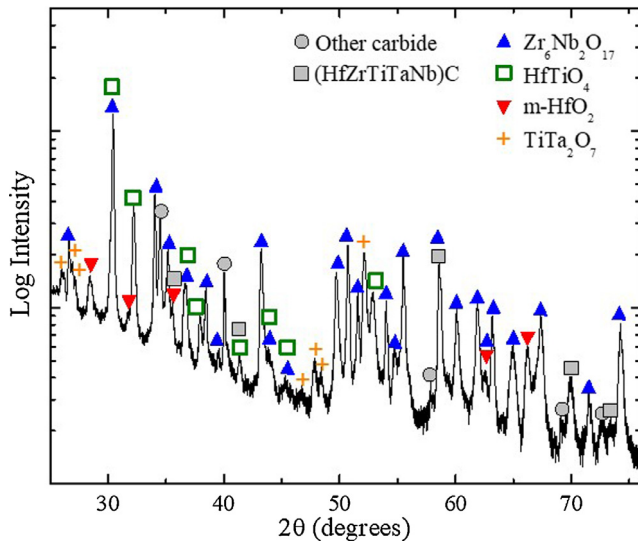


**Fig. 8.** X-ray diffraction spectra taken after oxidation for  $(\text{Hf}_{0.2}\text{Zr}_{0.2}\text{Ti}_{0.2}\text{Ta}_{0.2}\text{Nb}_{0.2})\text{C}$  exposed for 5 mins at a nominal temperature of  $1700^\circ\text{C}$  in 1 mol%  $\text{O}_2/\text{bal Ar}$ .

**Table 1**

Possible phase matches for the X-ray diffraction pattern (Fig. 8) collected from  $(\text{Hf}_{0.2}\text{Zr}_{0.2}\text{Ti}_{0.2}\text{Ta}_{0.2}\text{Nb}_{0.2})\text{C}$  oxidized at a nominal temperature of  $1700^\circ\text{C}$  in 1%  $\text{O}_2/\text{Ar}$  for 5 mins. PDF numbers or references are indicated in parentheses or brackets, respectively.

Indicated Phase	Crystal System	Possible alternate phases
$\text{Zr}_6\text{Nb}_2\text{O}_{17}$ (04–011–2890)	Orthorhombic	$(\text{Hf,Zr})_6(\text{Ta,Nb})_2\text{O}_{17}$ [22]
$\text{HfTiO}_4$ (01–080–2977)	Orthorhombic	$(\text{Hf,Zr})\text{TiO}_4$ [23]
$\text{HfO}_2$ (00–034–0104)	Monoclinic	$(\text{Hf,Zr})\text{O}_2$ [24,25]
$\text{TiTa}_2\text{O}_7$ (01–084–8891)	Monoclinic	$\text{Ti}(\text{Ta,Nb})_2\text{O}_7$ [26]
Other carbide	Cubic	$\text{NbC}_{0.92}\text{O}_{0.01}$ (04–022–7393) $\text{Nb}_{0.80}\text{Ta}_{0.20}\text{C}$ (01–085–4222) $\text{Zr}_{0.20}\text{Ta}_{0.80}\text{C}$ (04–002–6875) $\text{Nb}_x\text{C}_{x-1}$ [27] $\text{NbC}$ (00–038–1364) $\text{NbC}_{0.87}$ (04–008–3212)

cross-section, wherein the gas-oxide surface is underneath the carbon layer deposited during the FIB milling process. A white circle is added to an area of interest, which is a partially oxidized carbide grain. The oxygen lean areas correspond with an enrichment of Ta and Nb, whereas the oxygen rich areas, which are porous, are mostly rich in the group IV elements. Fig. 9 also shows the Ti-Ta rich oxide phases at the surface (Fig. 7), i.e., the gas-oxide interface, where the material is exposed to a higher  $p\text{O}_2$ , and where the carbide material has oxidized nearly to completion. Fig. 10 shows lower magnification images of the oxidized regions, characterized by porosity.

### 3.3. Borides: after oxidation

Fig. 11 shows low and high magnification BSE images of the oxide in plan view formed in the hot zone region of the diboride specimen, while Fig. 12 shows secondary electron images of the oxidized region in cross-section. In contrast to the carbide, the diboride specimen exhibits a uniform scale in plan view. This scale is composed largely of Hf, Zr and Ti, with very little Ta and almost no Nb. Directly beneath this scale is a region with oxides and partially oxidized diborides. These regions exhibit porosity filled with a phase that has morphology consistent with that solidified from a melt (Fig. 12), likely borria. Analysis of the FIB cross section (Fig. 13) taken from the oxidized  $(\text{Hf}_{0.2}\text{Zr}_{0.2}\text{Ti}_{0.2}\text{Ta}_{0.2}\text{Nb}_{0.2})\text{B}_2$  specimen shows that the surface oxide is dominated by Hf and Zr. Fig. 14 shows a detail image of partially oxidized boride grains approximately  $3\ \mu\text{m}$  below the surface, depleted in Hf and Zr. The oxide around these grains is rich in Hf, Zr and Ti. A Ti rich region in the grain is also observed. The interface between the Ti-rich region and the center of the grain, which is depleted in Ti and enriched in Ta and Nb, is distinct, indicating the possibility of different boride phases. XRD results shown in Fig. 15 and summarized in Table 2 confirm the preferential oxidation of group IV elements, and indicate the existence of a secondary group V rich boride.

### 3.4. Thermodynamic predictions

Table 3 shows the results for the free energy minimization calculation for  $(\text{Hf}_{0.2}\text{Zr}_{0.2}\text{Ti}_{0.2}\text{Ta}_{0.2}\text{Nb}_{0.2})\text{C}$  and  $(\text{Hf}_{0.2}\text{Zr}_{0.2}\text{Ti}_{0.2}\text{Ta}_{0.2}\text{Nb}_{0.2})\text{B}_2$  each in equilibrium with an equimolar solid solution

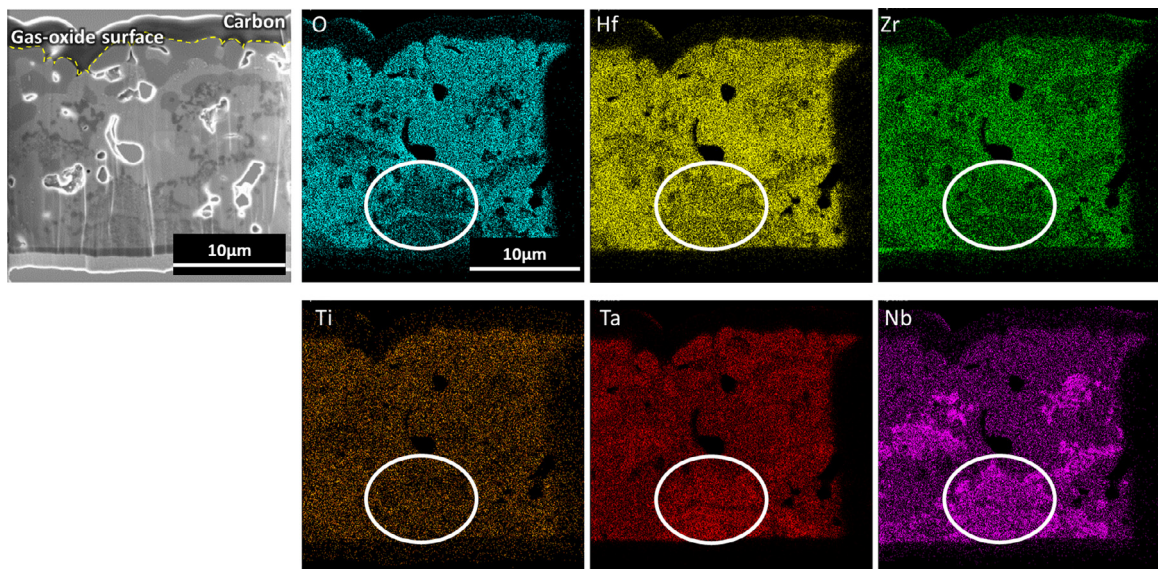


**Fig. 9.** FIB lift out from the hot zone in  $(\text{Hf}_{0.2}\text{Zr}_{0.2}\text{Ti}_{0.2}\text{Ta}_{0.2}\text{Nb}_{0.2})\text{C}$  oxidized for 5 mins at a nominal temperature of  $1700^\circ\text{C}$  in 1 mol%  $\text{O}_2/\text{bal Ar}$ . [Left] Secondary electron image of the focus ion beam (FIB) cross section of part of the oxide scale. [Right] EDS maps showing elemental distribution of oxygen, hafnium, zirconium, titanium, tantalum, and niobium. The white circle is added to help guide the eye to a partially oxidized grain.

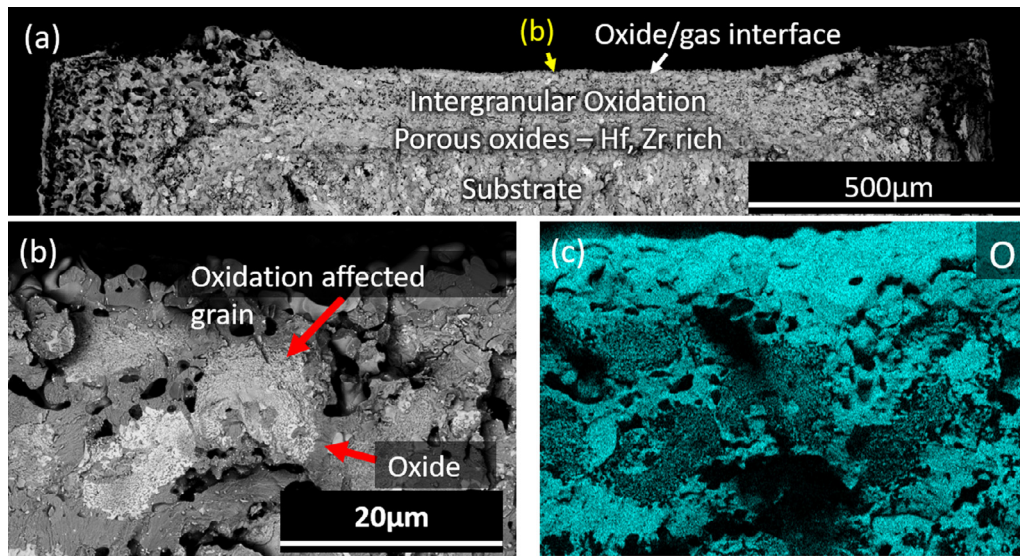


**Fig. 10.**  $(\text{Hf}_{0.2}\text{Zr}_{0.2}\text{Ti}_{0.2}\text{Ta}_{0.2}\text{Nb}_{0.2})\text{C}$  oxidized for 5 mins at a nominal temperature of 1700°C in 1 mol%  $\text{O}_2/\text{bal Ar}$ . (a) Low magnification back-scattered electron image of the top half of the sample fracture cross-section; (b) Higher magnification image of the oxidized carbide cross section at the location indicated in (a); Oxygen EDS map of the region shown in (b).

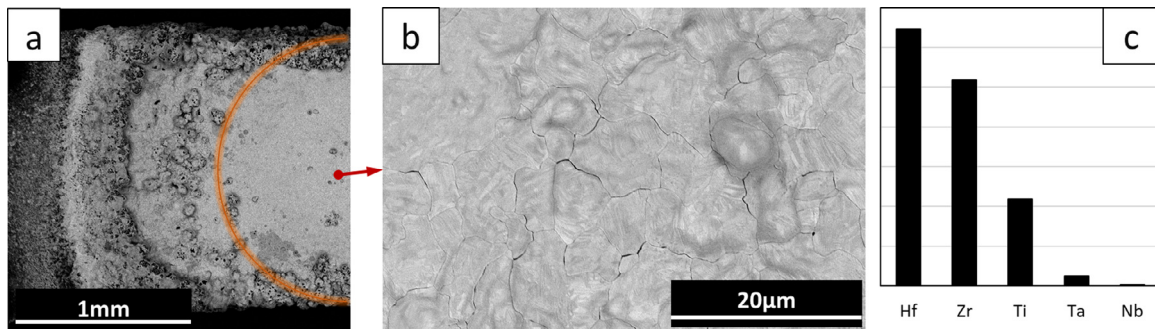


**Fig. 11.** (a) Back-scattered electron image showing the thin section of the  $(\text{Hf}_{0.2}\text{Zr}_{0.2}\text{Ti}_{0.2}\text{Ta}_{0.2}\text{Nb}_{0.2})\text{B}_2$  dogbone specimen oxidized for 5 mins at a nominal temperature of 1700°C in 1 mol%  $\text{O}_2/\text{bal Ar}$ ; the orange curve shows the approximate size and location of the hot zone in plan view. (b) Higher magnification plan view image of the microstructure in the pyrometer sighting zone. (c) Semi-quantitative EDS results for the elemental composition of the oxide in plan view.

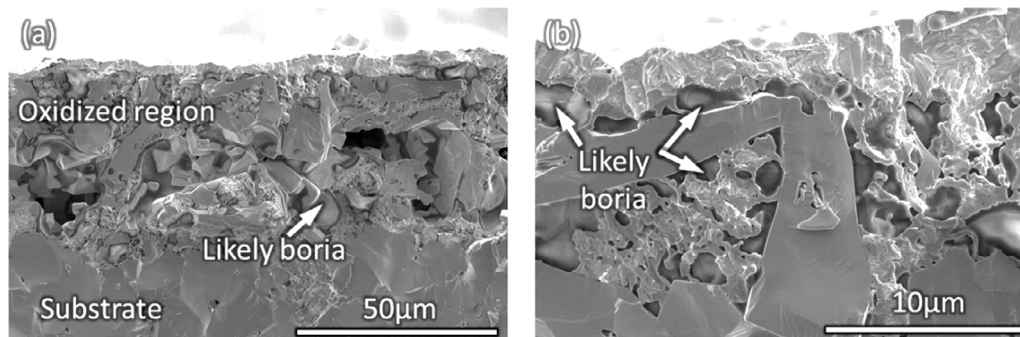


**Fig. 12.**  $(\text{Hf}_{0.2}\text{Zr}_{0.2}\text{Ti}_{0.2}\text{Ta}_{0.2}\text{Nb}_{0.2})\text{B}_2$  oxidized for 5 mins at a nominal temperature of 1700°C in 1 mol%  $\text{O}_2/\text{bal Ar}$ . (a) shows a lower magnification fracture cross-section secondary electron image of the microstructure; (b) shows a higher magnification image of the region near the oxide/gas interface.

containing  $\text{HfO}_2$ ,  $\text{ZrO}_2$ ,  $\text{TiO}_2$ ,  $\text{TaO}_{2.5}$ , and  $\text{NbO}_{2.5}$ , conducted at the experimental temperature, 1700°C. These thermodynamic predictions describe the local equilibrium at the carbide (or diboride) and oxide interface. Following the procedure described in detail in the companion paper [12], the calculation predicts the formation of an oxide primarily rich in the group IV elements (Hf, Zr and Ti), with Ta and Nb content in the oxide below experimentally determinable limits for both the carbide and the boride. Additionally,  $\text{CO}(\text{g})$  is predicted to form with a fugacity of 0.99 atm

for the carbide, while liquid boria is predicted to form for the diboride.

The calculation for the high entropy carbide resulted in the prediction of a carbon deficient group V carbide,  $\text{Nb}_8\text{C}_7$  ( $\text{NbC}_{0.87}$ ). Smith et al. [27] reported the diffraction patterns for a range of rock-salt sub-stoichiometric niobium carbides above  $\text{NbC}_{0.71}$  and found the X-ray diffraction peaks to occur at the same or similar 2-theta values as stoichiometric NbC. Therefore, the peaks corresponding to “other carbide” shown in Fig. 8 match multiple sub-

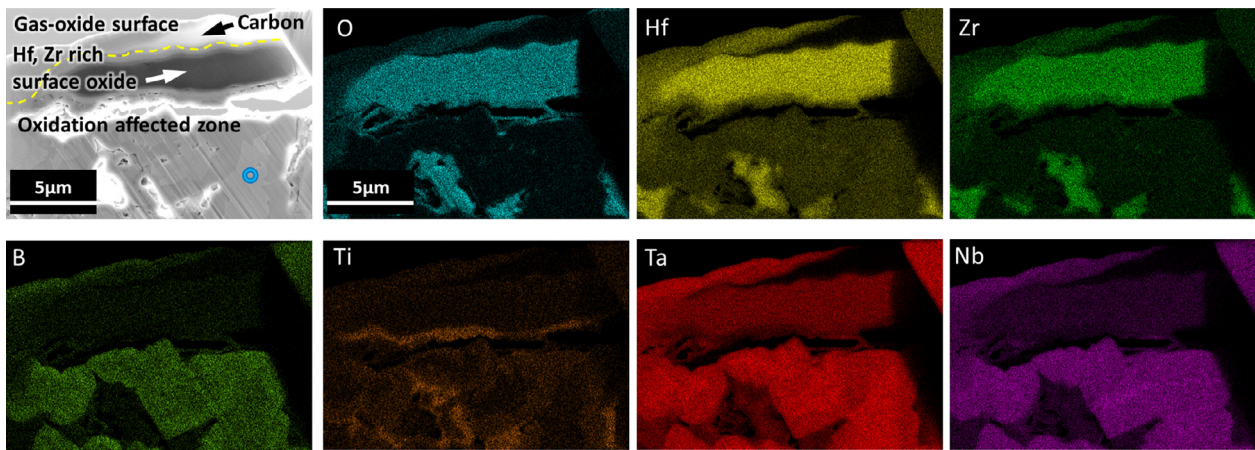


**Fig. 13.**  $(\text{Hf}_{0.2}\text{Zr}_{0.2}\text{Ti}_{0.2}\text{Ta}_{0.2}\text{Nb}_{0.2})\text{B}_2$  oxidized for 5 mins at a nominal temperature of 1700°C in 1 mol%  $\text{O}_2/\text{bal Ar}$ . Backscattered electron image in cross section of the top of the oxide scale at the hot zone, shown in the top left along with EDS maps showing elemental distribution of oxygen, hafnium, zirconium, boron, titanium, tantalum, and niobium. The blue circular marker indicates an area also shown in Fig. 14.

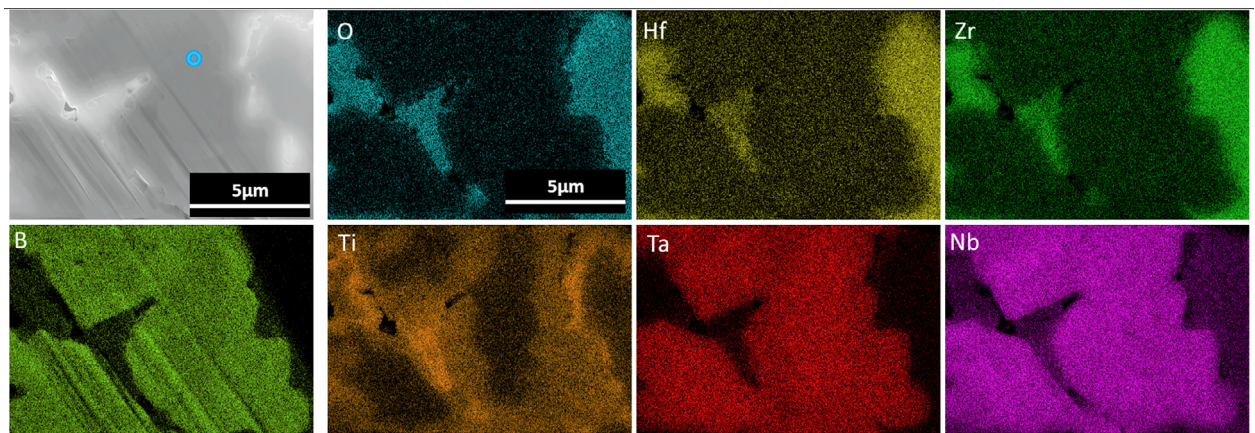


**Fig. 14.**  $(\text{Hf}_{0.2}\text{Zr}_{0.2}\text{Ti}_{0.2}\text{Ta}_{0.2}\text{Nb}_{0.2})\text{B}_2$  oxidized for 5 mins at a nominal temperature of 1700°C in 1 mol%  $\text{O}_2/\text{bal Ar}$ . [Left] Secondary electron image of the focus ion beam (FIB) cross section of part of the oxide scale 3  $\mu\text{m}$  below the surface in the hot zone, and EDS maps showing elemental distribution of oxygen, hafnium, zirconium, boron, titanium, tantalum, and niobium. The blue circular marker shown in Fig. 13 is repeated again here for reference.

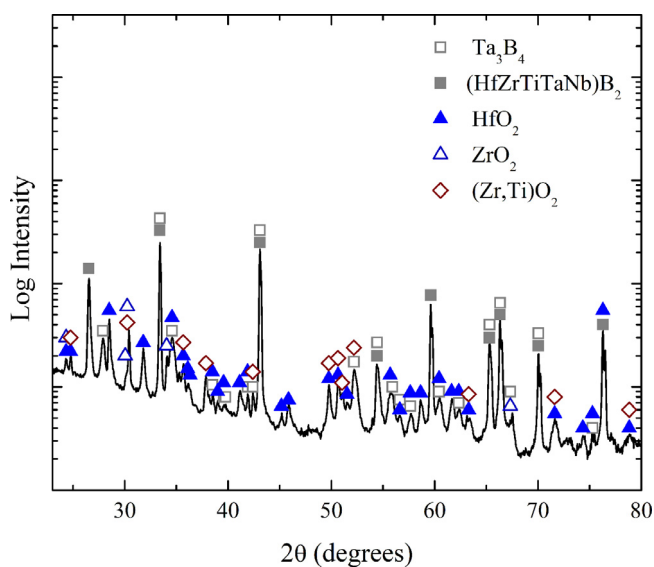


**Fig. 15.** X-ray diffraction spectra taken after oxidation for  $(\text{Hf}_{0.2}\text{Zr}_{0.2}\text{Ti}_{0.2}\text{Ta}_{0.2}\text{Nb}_{0.2})\text{B}_2$  oxidized for 5 mins at a nominal temperature of 1700°C in 1 mol%  $\text{O}_2/\text{bal Ar}$ .

**Table 2**

Possible phase matches for the X-ray diffraction pattern (Fig. 15) collected from  $(\text{Hf}_{0.2}\text{Zr}_{0.2}\text{Ti}_{0.2}\text{Ta}_{0.2}\text{Nb}_{0.2})\text{B}_2$  oxidized for five minutes at a nominal temperature of 1700°C in 1 mol%  $\text{O}_2/\text{bal Ar}$ . PDF numbers or references are indicated in parentheses or brackets, respectively.

Indicated Phase	Crystal System	Possible alternate phases/overlaps
$\text{HfO}_2$ (00–034–0104)	Monoclinic	$(\text{Hf, Zr})\text{O}_2$ [24,25] $(\text{Hf, Zr,Ti})\text{O}_2$ [23]
$\text{ZrO}_2$ (00–042–1164)	Tetragonal	$(\text{Hf, Zr})\text{O}_2$ [24,25] $(\text{Hf, Zr,Ti})\text{O}_2$ [23]
$(\text{Zr, Ti})\text{O}_2$ (04–002–8273)	Orthorhombic	$(\text{Hf, Zr,Ti})\text{O}_2$ [23] $(\text{Hf, Zr,Ti})\text{O}_2$ [23]
$\text{Ta}_3\text{B}_4$ (04–003–3812)	Orthorhombic	$(\text{Hf, Zr,Ti})\text{O}_2$ [23] $(\text{Nb,Ta})_3\text{B}_4$ [26,28]

stoichiometric niobium carbide reference patterns, hence the multiple possibilities indicated in Table 1.

#### 4. Discussion

##### 4.1. Comparison of experimental results to calculated predictions

The computational results shown in Table 3 predict the oxidation of group IV elements is thermodynamically favored and therefore preferentially oxidize, consistent with Part I of this work. As discussed in the companion publication [12], the thermodynamic prediction for the oxidized diborides are similar to that of the

**Table 3**

Equilibrium calculations showing the final composition of the oxide scale and underlying substrate that results from an inputs of equimolar quinary alloy ( $\text{Hf}_{0.2}\text{Zr}_{0.2}\text{Ti}_{0.2}\text{Ta}_{0.2}\text{Nb}_{0.2}\text{C}$ ) and ( $\text{Hf}_{0.2}\text{Zr}_{0.2}\text{Ti}_{0.2}\text{Ta}_{0.2}\text{Nb}_{0.2}\text{B}_2$ ), respectively, at 1700 °C in equilibrium with an equimolar (cation atom basis) oxide ideal solid solution containing  $\text{HfO}_2$ ,  $\text{ZrO}_2$ ,  $\text{TiO}_2$ ,  $\text{Ta}_2\text{O}_5$ ,  $\text{Nb}_2\text{O}_5$ . † indicates separate phases predicted to form but that were not part of the substrate or oxide solid solution.

Constituents	Input (mol)	Input (mol%)	Carbide Output (mol%)	Boride Output (mol%)
<b>Carbide/Boride Ideal Solution</b>				
Hf	1	20	0.015	0.025
Zr	1	20	0.022	0.180
Ti	1	20	14.1	15.5
Ta	1	20	44.7	42.2
Nb	1	20	41.1	42.2
$\text{Nb}_8\text{C}_7$	–	–	†	–
<b>CO (g)</b>	–	–	†(0.99 atm)	–
<b><math>\text{B}_2\text{O}_3</math> (l)</b>	–	–	–	†
<b>Oxide Ideal Solution</b>				
$\text{HfO}_2$	1	20	39.9	42.7
$\text{ZrO}_2$	1	20	39.9	42.6
$\text{TiO}_2$	1	20	20.2	8.50
$\text{Ti}_3\text{O}_5$	–	–	–	6.19
$\text{Ta}_{2.5}$	1	20	$8.22 \times 10^{-4}$	$9.89 \times 10^{-3}$
$\text{Nb}_{2.5}$	1	20	$4.38 \times 10^{-7}$	$5.32 \times 10^{-9}$
<b>Equilibrium <math>p\text{O}_2</math></b>	–	–	$2.55 \times 10^{-13}$	$3.70 \times 10^{-13}$

carbides, except that secondary, condensed phase,  $\text{B}_2\text{O}_3$  (l), may also form, albeit with a high vapor pressure ( $\sim 10^{-2}$  atm). The formation of a carbon-poor, Nb rich carbide phase is also predicted for the carbide system, in addition to the original rock-salt carbide phase. The formation of such a phase outside of the rock-salt carbide phase may be an artifact of the thermodynamic database used; prior studies or databases for carbides in the Nb-C system [27,29,30] do not have data for  $\text{Nb}_8\text{C}_7$ . A stoichiometry of 1:0.87 (Nb:C) in the phase diagram [29] at the test temperature indicates that the equilibrium phase is carbon-deficient NbC. High temperature oxidation studies of niobium carbide have been observed to result in preferential oxidation of carbon [31], leading to metal-rich compositions; Smith et al. [27] have observed that for  $\text{NbC}_x$  where  $x \leq 0.63$ , the niobium carbide adopts a trigonal structure.

The experimental observations are in good agreement with the calculated predictions for the oxide composition formed on the carbide and the diboride at the substrate/oxide interface: the group IV elements preferentially oxidize over the group V elements, while the substrate is enriched in group V elements. Within these groups, the extent of oxidation of the different elements also corresponds to their oxide thermodynamic favorability. Hf and Zr, which form the most stable oxides, oxidize preferentially, followed by Ti. Of the group V elements,  $\text{Ta}_2\text{O}_5$  is more stable than  $\text{Nb}_2\text{O}_5$ , and thus Ta is expected to preferentially oxidize over Nb.

The combination of intergranular oxidation and preferential oxidation would result in an oxide scale with an evolving composition until the grain is completely consumed. This explains the other phases formed after oxidation of the carbide and detected via XRD (Fig. 8, Table 1) on the specimen surface where the oxidation of grains has gone to completion or near completion. The Ta content in the oxide formed on the carbide is higher than both the calculated predictions and the experimental observations for the oxidized boride. Oxidized regions with higher Ta content than predicted by the thermodynamic calculations were observed in regions farther away from the carbide/oxide interface. As the group IV elements are depleted, the substrate becomes group V rich; further oxidation of the grains therefore results in the incorporation of Ta in the oxides. Comparison of the oxidation of the carbides and diborides indicate that this occurred for the carbide for the oxidation conditions studied in this work, but not the diboride. The porous, intergranular oxides formed on the carbide (Figs. 9 and 10)

is attributed to the formation and release of  $\text{CO}(\text{g})$  [32,33], which is the dominant gaseous oxide product formed upon oxidation of the carbide (Table 3). In comparison, the formation and retention of liquid boron attending the oxidation of diborides at this temperature may seal pores and defects in the oxide and result in a more effective barrier to oxidant ingress [2,34,35] compared to the gas-filled pores in the carbide case. Such a pore-filling phase was observed (Fig. 12) in the oxidized diboride beneath the group IV-rich scale. The composition of this phase was indeterminate via EDS analysis due to low counts. The morphology of this phase is consistent with solidification from a melt, and is inferred to be liquid boron, which is known to be retained in the scale of oxidized diborides up to 1800°C [35]. Other possible oxide or boride phases as determined from EDS and XRD (Fig. 15, Table 2) do not have melting temperatures at or below 1700°C.

The formation of a porous scale upon oxidation of the carbide also results in higher oxygen partial pressures at the reaction interface in the carbide, which allows for the further oxidation of Ta over Nb ( $\text{Ta}_2\text{O}_5$  is more stable than  $\text{Nb}_2\text{O}_5$ ). Fig. 7 and the EDS maps in Fig. 11 show that Ta is present in some of the oxygen rich regions, but almost no Nb. XRD matches for Nb-rich carbides are consistent with this interpretation and calculated predictions. In contrast, the dense surface scale formed on the diboride and filled pores likely reduces the oxygen partial pressure at the reaction interface. This explains not only the predicted low tantalum content in the oxide formed on the diborides, but also the titanium retained in the boride phase in Figs. 11 and 12. Hf and Zr oxides are significantly more thermodynamically stable than  $\text{TiO}_2$  (see Ellingham diagram in companion paper [12]); Hf and Zr oxidize preferentially from the boride, leading to Ti “lagging” the other group IV elements in extent of oxidation. The depletion zone in the Ti map (Fig. 15) indicates that some Ti is still retained in the diboride. The  $\text{Ta}_3\text{B}_4$  boride phase indicated by the XRD results is consistent with a tantalum rich composition, an analog to Nb rich substoichiometric carbide in the high entropy carbide case.

#### 4.2. Complex oxide formation

The preceding work and that outlined in the companion paper are predicated on the assumption that the carbide or boride is in equilibrium with a solid solution oxide. The lack of available thermodynamic data for complex or ordered compounds limited consideration of these phases. A review of the relevant phase diagrams indicate that only Hf- and Zr- oxides exhibit complete solubility. Other binary and/or ternary oxide systems under consideration exhibit only partial solid solubility and complex oxide formation. Further, the XRD patterns for the oxidized samples indicate that oxide compounds such as  $\text{Zr}_6\text{Nb}_2\text{O}_{17}$  and  $(\text{Hf,Zr})\text{TiO}_4$  formed. Table 4 summarizes known complex oxides which are likely to form based on a review of the available phase diagrams. As presented in Section 3, the actual oxides formed on the high entropy ceramics are complex variations of the compounds shown in Table 4, due to the possibility of ionic substitutions. For example, Hf and Zr are known to form substitutional solid solutions in alloys and oxides, and in their computational work, Hautier et al. [26] found that Ta and Nb have a high likelihood to substitute for each other. In fact, an analogous phase to  $\text{Zr}_6\text{Nb}_2\text{O}_{17}$  exists with Hf and Ta:  $\text{Hf}_6\text{Ta}_2\text{O}_{17}$  [22,36].

It has been posited by Butler et al. [9] and Gorr et al. [37] that the formation of complex oxide phases may promote improved oxidation resistance, and therefore be an advantage of high entropy materials relative to conventional alloys and ceramics. Consideration of the complex oxide phases was outside the scope of this work, largely due to the lack of thermodynamic data. However, it can be seen from the experimental results that despite the formation of complex oxides, the elemental composition of the as-

**Table 4**  
Known complex oxides that could form in the material systems under study, based on a review of available phase diagrams.

	Hf	Ti	Zr	Nb	Ta
<b>Hf</b>					
<b>Ti</b>	HfTiO <sub>4</sub> [38]				
<b>Zr</b>		ZrTiO <sub>4</sub> [23,39,40]			
<b>Nb</b>	Hf <sub>6</sub> Nb <sub>2</sub> O <sub>17</sub> [41]	Nb <sub>2</sub> TiO <sub>7</sub> [42] Nb <sub>10</sub> Ti <sub>2</sub> O <sub>29</sub> [42] Nb <sub>6</sub> Ti <sub>2</sub> O <sub>19</sub> [42] TiNb <sub>6</sub> O <sub>17</sub> [43]	Zr <sub>6</sub> Nb <sub>2</sub> O <sub>17</sub> [43]		
<b>Ta</b>	Hf <sub>6</sub> Ta <sub>2</sub> O <sub>17</sub> [36]	TiTa <sub>2</sub> O <sub>7</sub> [21]	ZrTa <sub>6</sub> O <sub>17</sub> [44] Zr <sub>6</sub> Ta <sub>2</sub> O <sub>19</sub> [44]	Nb <sub>4</sub> Ta <sub>2</sub> O <sub>15</sub> [45]	
<b>V</b>			ZrV <sub>2</sub> O <sub>7</sub> [46]	VNb <sub>9</sub> O <sub>25</sub> [47]	VTa <sub>9</sub> O <sub>25</sub> [48,49]
<b>Mo</b>					
<b>W</b>	HfW <sub>2</sub> O <sub>8</sub> [50]		ZrW <sub>2</sub> O <sub>8</sub> [50]		

semblage of oxides still followed the predicted trend, wherein the group IV elements oxidized preferentially and dominated the composition of the thermally grown oxide.

#### 4.3. Implications for use of HE-UHTCs in oxidizing environments

Oxides formed from group IV elements (Hf, Zr, Ti) have the highest melting temperatures ( $T_m$ ) and are most thermodynamically favored among the refractory elements. The predicted and observed preferential oxidation of these elements demonstrate that an HE-UHTC can be designed to form an oxide scale containing these elements. Further, the retention of elements with low  $T_m$  oxides as carbides or borides ensures a material with a high thermal stability overall, as Nb and Ta carbides and borides have melting temperatures greater than 2000°C [51]. The approach outlined in Part I and this work can further be used to optimize such a composition as a multi-principal component material that is not equimolar, but promotes a targeted oxide and substrate composition.

On the other hand, the preferential depletion of several elements from the substrate can destabilize the underlying substrate and promote the formation of other phases. This destabilization can result in the loss of properties that might be gained from the high entropy design concept.

## 5. Conclusions

The objective of this work was to experimentally test the predictions of the analytical and computational thermodynamic approach outlined in a companion publication. This methodology was applied to the prediction of substrate and oxide composition after oxidation of a high entropy carbide and boride containing Hf, Zr, Ti, Ta and Nb in equimolar amounts. The experimentally determined oxide and substrate compositions were found to be in good agreement with the thermodynamic predictions, which describe well the local equilibrium at the reaction interface for both the carbide and the diboride case. In general, the oxidation of high entropy materials studied here occurred by preferential oxidation of each component according to the relative thermodynamic favorabilities of their respective oxides. Group IV oxides, being most favorable, formed preferentially. The experimental results further elucidated that within each group, preferential oxidation can also occur according to relative thermodynamic stability: Hf and Zr preferentially oxidize over Ti as shown in the boride case, while Ta preferentially oxidizes over Nb as shown in the carbide case. The substrate composition of group V metal-rich carbides and borides, which are or have the potential to form phases with different crystal structures from the original ceramic, was accurately predicted. Whereas complex oxides were observed experimentally, this is not a significant limitation to the prediction of preferential oxidation,

as the formation of these complex oxides was dominated by predicted oxide constituents.

This work shows that the approach outlined in Part I provides insight into the thermodynamics driving the oxidation behavior of high entropy materials and can be used as a tool for the design of high entropy materials for oxidation resistance.

## Declaration of Competing Interest

The authors declare that they have no known competing financial interests or personal relationships that could have appeared to influence the work reported in this paper.

## Acknowledgments

This work is supported by the U.S. Office of Naval Research MURI program (grant no. N00014-15-1-2863) and the Virginia Space Grant Consortium Graduate Research Fellowship. Bulk carbide samples were provided by the Vecchio research group at the University of California San Diego. The authors would also like to thank Professors Bill Fahrenholtz (Missouri University of Science and Technology), Bill Soffa, Bi-Cheng Zhou (University of Virginia) and Christina Rost (James Madison University) for helpful discussions, and Dr. Helge Heinrich (University of Virginia) for help with the FIB lift-outs. Characterization was conducted at the Nanoscale Materials Characterization Facility at University of Virginia.

## Supplementary materials

Supplementary material associated with this article can be found, in the online version, at doi:10.1016/j.actamat.2020.07.004.

## References

- [1] D. Glass, Physical challenges and limitations confronting the Use of UHTCs on hypersonic vehicles, in: Proceedings of the 17th AIAA International Space Planes and Hypersonic Systems and Technologies Conference, American Institute of Aeronautics and Astronautics, 2011, doi:10.2514/6.2011-2304.
- [2] E. Wuchina, E. Opila, M. Opeka, W. Fahrenholtz, I. Talmay, UHTCs: ultra-high temperature ceramic materials for extreme environment applications, *Electrochem. Soc. Interface* 16 (2007) 30.
- [3] A. Paul, D.D. Jayaseelan, S. Venugopal, E. Zapata-Solvas, J.G.P. Binner, B. Vaidyanathan, A. Heaton, P.M. Brown, W.E. Lee, UHTC composites for hypersonic applications, (2012). <https://dspace.lboro.ac.uk/dspace-jspui/handle/2134/9676> (accessed August 26, 2016).
- [4] M.M. Opeka, I.G. Talmay, J.A. Zaykoski, Oxidation-based materials selection for 2000°C + hypersonic aerosurfaces: theoretical considerations and historical experience, *J. Mater. Sci.* 39 (2004) 5887–5904, doi:10.1023/B:JMSC.0000041686.21788.77.
- [5] E. Wuchina, M. Opeka, S. Causey, K. Buesking, J. Spain, A. Cull, J. Routbort, F. Guitierrez-Mora, Designing for ultrahigh-temperature applications: the mechanical and thermal properties of HfB<sub>2</sub>, HfC<sub>x</sub>, HfN<sub>x</sub> and αHf(N), *J. Mater. Sci.* 39 (2004) 5939–5949, doi:10.1023/B:JMSC.0000041690.06117.34.
- [6] J. Gild, Y. Zhang, T. Harrington, S. Jiang, T. Hu, M.C. Quinn, W.M. Mellor, N. Zhou, K. Vecchio, J. Luo, High-Entropy Metal Diborides, A New Class of

- High-Entropy Materials and a New Type of Ultrahigh Temperature Ceramics, *Sci. Rep.* 6 (2016), doi:10.1038/srep37946.
- [7] J. Gild, J. Braun, K. Kaufmann, E. Marin, T. Harrington, P. Hopkins, K. Vecchio, J. Luo, A high-entropy silicide:  $(\text{Mo}_{0.2}\text{Nb}_{0.2}\text{Ta}_{0.2}\text{Ti}_{0.2}\text{W}_{0.2})\text{Si}_2$ , *J. Mater.* (2019), doi:10.1016/j.jmat.2019.03.002.
- [8] E. Castle, T. Csanádi, S. Grasso, J. Dusza, M. Reece, Processing and Properties of High-Entropy Ultra-High Temperature Carbides, *Sci. Rep.* 8 (2018) 8609, doi:10.1038/s41598-018-26827-1.
- [9] T.M. Butler, K.J. Chaput, J.R. Dietrich, O.N. Senkov, High temperature oxidation behaviors of equimolar NbTiZrV and NbTiZrCr refractory complex concentrated alloys (RCCAs), *J. Alloys Compd.* 729 (2017) 1004–1019, doi:10.1016/j.jallcom.2017.09.164.
- [10] B. Gorr, F. Müller, M. Azim, H.-J. Christ, T. Müller, H. Chen, A. Kauffmann, M. Heilmaier, High-temperature oxidation behavior of refractory high-entropy alloys: effect of alloy composition, *Oxid Met* (2017) 1–11, doi:10.1007/s11085-016-9696-y.
- [11] L. Backman, E.J. Opila, Thermodynamic assessment of the group IV, V and VI oxides for the design of oxidation resistant multi-principal component materials, *J. Eur. Ceram. Soc.* 39 (2019) 1796–1802, doi:10.1016/j.jeurceramsoc.2018.11.004.
- [12] Lavina Backman, Joshua Gild, Jian Luo, Elizabeth J. Opila, Part I: Theoretical predictions of preferential oxidation of refractory high entropy materials, *Acta Materialia* (2020) In press, doi:10.1016/j.actamat.2020.07.003.
- [13] E. Opila, S. Levine, J. Lorincz, Oxidation of ZrB<sub>2</sub>- and HfB<sub>2</sub>-based ultra-high temperature ceramics: effect of Ta additions, *J. Mater. Sci.* 39 (2004) 5969–5977, doi:10.1023/B:JMSC.0000041693.32531.d1.
- [14] L. Silvestroni, D. Sciti, M. Balat-Pichelin, L. Charpentier, Zirconium carbide doped with tantalum silicide: microstructure, mechanical properties and high temperature oxidation, *Mater. Chem. Phys.* 143 (2013) 407–415, doi:10.1016/j.matchemphys.2013.09.020.
- [15] O. Cedillos-Barraza, D. Manara, K. Boboridis, T. Watkins, S. Grasso, D.D. Jayaseelan, R.J.M. Konings, M.J. Reece, W.E. Lee, Investigating the highest melting temperature materials: a laser melting study of the TaC-HfC system, *Sci. Rep.* 6 (2016) 37962, doi:10.1038/srep37962.
- [16] T.J. Harrington, J. Gild, P. Sarker, C. Toher, C.M. Rost, O.F. Dippo, C. McElfresh, K. Kaufmann, E. Marin, L. Borowski, P.E. Hopkins, J. Luo, S. Curtarolo, D.W. Brenner, K.S. Vecchio, Phase stability and mechanical properties of novel high entropy transition metal carbides, *Acta Mater.* 166 (2019) 271–280, doi:10.1016/j.actamat.2018.12.054.
- [17] P. Sarker, T. Harrington, C. Toher, C. Oses, M. Samiee, J.-P. Maria, D.W. Brenner, K.S. Vecchio, S. Curtarolo, High-entropy high-hardness metal carbides discovered by entropy descriptors, *Nat Commun.* 9 (2018) 1–10, doi:10.1038/s41467-018-07160-7.
- [18] J. Gild, A. Wright, K. Quiambao-Tomko, M. Qin, J.A. Tomko, M. Shafkat, bin Hoque, J.L. Braun, B. Bloomfield, D. Martinez, T. Harrington, K. Vecchio, P.E. Hopkins, J. Luo, Thermal conductivity and hardness of three single-phase high-entropy metal diborides fabricated by borocarbothermal reduction and spark plasma sintering, *Ceram. Int.* (2019), doi:10.1016/j.ceramint.2019.11.186.
- [19] S.N. Karlsdottir, J.W. Halloran, Rapid oxidation characterization of ultra-high temperature ceramics, *J. Am. Ceramic Soc.* 90 (2007) 3233–3238, doi:10.1111/j.1551-2916.2007.01861.x.
- [20] K. Shugart, E. Opila, SiC Depletion in ZrB<sub>2</sub>-30 vol% SiC at Ultrahigh Temperatures, *J. Am. Ceramic Soc.* 98 (2015) 1673–1683, doi:10.1111/jace.13519.
- [21] J.L. Waring, R.S. Roth, Effect of oxide additions on polymorphism of tantalum pentoxide (system Ta<sub>2</sub>O<sub>5</sub>-TiO<sub>2</sub>), *J. Res. Natl. Bureau Stand. Sect. A Phys. Chem.* 72A (1968) 175, doi:10.6028/jres.072A.018.
- [22] S.J. McCormack, W.M. Kriven, Crystal structure solution for the A<sub>6</sub>B<sub>2</sub>O<sub>17</sub> (A = Zr, Hf; B = Nb, Ta) superstructure, *Acta Cryst. B* 75 (2019) 227–234, doi:10.1107/S2052520619001963.
- [23] Phase Equilibria Diagrams Online Database (NIST Standard Reference Database 31), The American Ceramic Society and the National Institute of Standards and Technology, 2020. Figure Numbers EC-701; [www.nist.gov/srd/nist31.cfm](http://www.nist.gov/srd/nist31.cfm).
- [24] V.V. Kharton, A.A. Yaremchenko, E.N. Naumovich, F.M.B. Marques, Research on the electrochemistry of oxygen ion conductors in the former Soviet Union, *J. Solid State Electrochem.* 4 (2000) 243–266, doi:10.1007/s100080050202.
- [25] R. Ruh, H.J. Garrett, R.F. Domagala, N.M. Tallan, The System Zirconia-Hafnia, *J. Am. Ceramic Soc.* 51 (1968) 23–28, doi:10.1111/j.1151-2916.1968.tb11822.x.
- [26] G. Hautier, C. Fischer, V. Ehrlicher, A. Jain, G. Ceder, Data mined ionic substitutions for the discovery of new compounds, *Inorg. Chem.* 50 (2011) 656–663.
- [27] C.J. Smith, C.R. Weinberger, G.B. Thompson, Phase stability and microstructural formations in the niobium carbides, *J. Eur. Ceram. Soc.* 38 (2018) 4850–4866, doi:10.1016/j.jeurceramsoc.2018.06.041.
- [28] A. Prokhorov, N. Lyakishev, G. Burkhanov, V. Dement'ev, High-purity transition metal borides: promising materials for present-day technology, *Neorganicheskie Materialy* 32 (1996) 1365–1371.
- [29] A.I. Gusev, Order-disorder transformations and phase equilibria in strongly nonstoichiometric compounds, *Phys. Usp.* 43 (2000) 10.1070/PU2000v043n01ABEH000647.
- [30] C. Oses, E. Gossett, D. Hicks, F. Rose, M.J. Mehl, E. Perim, I. Takeuchi, S. Sanvito, M. Scheffler, Y. Lederer, O. Levy, C. Toher, S. Curtarolo, AFLOW-CHULL: cloud-oriented platform for autonomous phase stability analysis, *J. Chem. Inf. Model.* 58 (2018) 2477–2490, doi:10.1021/acs.jcim.8b00393.
- [31] A. Szokefalvi-Nagy, H. Jehn, High-temperature oxidation of NbC and TaC at low oxygen pressures, *Z. Metallkd.* 75 (1984) 389–394.
- [32] E.J. Wuchina, M. Opeka, The Group IV Carbides and Nitrides, in: *Ultra-High Temperature Ceramics*, John Wiley & Sons, Ltd, 2014, pp. 361–390, doi:10.1002/9781118700853.ch14.
- [33] E.L. Courtright, J.T. Prater, G.R. Holcomb, G.R. St. Pierre, R.A. Rapp, Oxidation of hafnium carbide and hafnium carbide with additions of tantalum and praseodymium, *Oxid Met* 36 (1991) 423–437, doi:10.1007/BF01151590.
- [34] A.G. Metcalfe, Gas Evolution During Oxidation of Refractory Borides and Carbides at 1500°C to 2700°C, *ECS Trans* 3 (2007) 131–142, doi:10.1149/1.2721464.
- [35] T.A. Parthasarathy, R.A. Rapp, M. Opeka, R.J. Kerans, A model for the oxidation of ZrB<sub>2</sub>, HfB<sub>2</sub> and TiB<sub>2</sub>, *Acta Mater* 55 (2007) 5999–6010 <https://doi.org/10.1016/j.actamat.2007.07.027>.
- [36] S.J. McCormack, K.-P. Tseng, R.J.K. Weber, D. Kapush, S.V. Ushakov, A. Navrotsky, W.M. Kriven, In-situ determination of the HfO<sub>2</sub>-Ta<sub>2</sub>O<sub>5</sub>-temperature phase diagram up to 3000°C, *J. Am. Ceramic Soc.* 102 (2019) 4848–4861, doi:10.1111/jace.16271.
- [37] F. Müller, B. Gorr, H.-J. Christ, J. Müller, B. Butz, H. Chen, A. Kauffmann, M. Heilmaier, On the oxidation mechanism of refractory high entropy alloys, *Corros Sci* 159 (2019) 108161, doi:10.1016/j.corsci.2019.108161.
- [38] J.P. Coutures, J. Coutures, The System HfO<sub>2</sub>-TiO<sub>2</sub>, *J. Am. Ceramic Soc.* 70 (1987) 383–387, doi:10.1111/j.1151-2916.1987.tb05655.x.
- [39] T. Noguchi, M. Mizuno, Phase Changes in the ZrO<sub>2</sub>-TiO<sub>2</sub> System, *BCSJ* 41 (1968) 2895–2899, doi:10.1246/bcsj.41.2895.
- [40] A.E. McHale, R.S. Roth, Investigation of the Phase Transition in ZrTiO<sub>4</sub> and ZrTiO<sub>4</sub>-SnO<sub>2</sub> Solid Solutions, *J. Am. Ceramic Soc.* 66 (1983) C-18-C-20, doi:10.1111/j.1151-2916.1983.tb09997.x.
- [41] Phase Equilibria Diagrams Online Database (NIST Standard Reference Database 31), The American Ceramic Society and the National Institute of Standards and Technology, 2020. Figure Number EC-229; [www.nist.gov/srd/nist31.cfm](http://www.nist.gov/srd/nist31.cfm).
- [42] A. Jongejan, A. Wilkins, A re-examination of the system Nb<sub>2</sub>O<sub>5</sub>-TiO<sub>2</sub> at liquidus temperatures, *J. Less Common Metals* 19 (1969) 185–191.
- [43] R.S. Roth, L.W. Coughanour, Phase equilibrium relations in the systems titania-niobia and zirconia-niobia, *J. Res. Natl. Bur. Stand.* (1934) 55 (1955) 209, doi:10.6028/jres.055.023.
- [44] R. Roth, J. Waring, Effect of oxide additions on the polymorphism of tantalum pentoxide III. Stabilization of the low temperature structure type, *J. Res. Natl. Bureau Stand. A Phys. Chem.* (1970) 485–493.
- [45] F. Holtzberg, A. Reisman, Sub-Solidus Equilibria in the System Nb<sub>2</sub>O<sub>5</sub>-Ta<sub>2</sub>O<sub>5</sub>, *J. Phys. Chem.* 65 (1961) 1192–1196, doi:10.1021/j100825a024.
- [46] E.M. Levin, C.R. Robbins, H.F. McMurdie, M.K. Reser, Phase diagrams for ceramists: 1969 supplement: [figure 2405], *American Ceramic Society*, 1969.
- [47] J. Waring, R. Roth, Phase equilibria in the system vanadium oxide-niobium oxide, *J. Res. Natl. Bur. Std.* 69 (1965).
- [48] R.S. Roth, J.L. Waring, W.S. Brower, Effect of oxide additions on the polymorphism of tantalum pentoxide. II. "Stabilization" of the high temperature structure type, *J. Res. Natl. Bureau Stand. Sect. A Phys. Chem.* 74A (1970) 477–484, doi:10.6028/jres.074A.037.
- [49] H. Schadow, H. Oppermann, B. Wehner, Investigations on the Quasi-binary System V<sub>2</sub>O<sub>5</sub>-Ta<sub>2</sub>O<sub>5</sub>, *Crystal Res. Technol.* 27 (1992) 691–695.
- [50] L.L. Chang, M. Scroger, B. Phillips, Condensed phase relations in the systems ZrO<sub>2</sub>-WO<sub>2</sub>-WO<sub>3</sub> and HfO<sub>2</sub>-WO<sub>2</sub>-WO<sub>3</sub>, *J. Am. Ceramic Soc.* 50 (1967) 211–215.
- [51] E. Rudy, Ternary phase equilibria in transition metal- boron-carbon-silicon systems. Part 5- Compendium of phase diagram data Summary report, 1 Jan. 1964- 30 Apr. 1969 (Phase diagrams of binary transition metal systems and binary and ternary systems of refractory metal alloys), (1969).